ACS Photonics

pubs.acs.org/journal/apchd5

Article

Giant Quantum Yield Enhancement in CdS/MgF_2/Ag Hybrid Nanobelt under Two-Photon Excitation

Xiangyuan Xing, Kai Wang,* Xiaobo Han, Shuhang Qian, Kun Wang, Hua Long, Bing Wang, and Peixiang Lu*

Cite This: *ACS Photonics* 2020, 7, 2987−2994

Read Online

ACCESS | Metrics & More | Article Recommendations | Supporting Information

ABSTRACT: We demonstrate a giant quantum yield (QY) enhancement (230 times) in a single CdS/MgF_2/Ag hybrid nanobelt under the two-photon excitation at 800 nm. The power-dependent two-photon photoluminescence (TPL) and the time-resolved photoluminescence (TRPL) measurement are performed in a single half-covered CdS/MgF_2/Ag nanobelt, offering a direct comparison between the CdS nanobelt with and without MgF_2/Ag coating. The quantitative theoretical analysis based on the free carrier dynamic model indicates the defect concentration is reduced from $(3.7 \pm 0.9) \times 10^{19}$ cm^{-3} (in bare) to $(3.9 \pm 0.6) \times 10^{18}$ cm^{-3} (in hybrid CdS nanobelt) due to the surface passivation, and the radiative recombination rate is increased from $(1.7 \pm 0.2) \times 10^{-11}$ cm^3 s^{-1} (in bare) to $(7.1 \pm 1.3) \times 10^{-11}$ cm^3 s^{-1} (in hybrid CdS nanobelt) due to the Purcell effect. Moreover, combined with the enhancement of the local field at the excitation wavelength (6.3×) and the signal collection efficiency (1.42×), a total 1800× enhancement of the TPL signal is achieved in experiment. Our work provides a quantitative characterization on free carrier dynamics of the surface defect passivation in semiconductor nanostructures, which has potentials in photovoltaics and photodetectors with high performance.

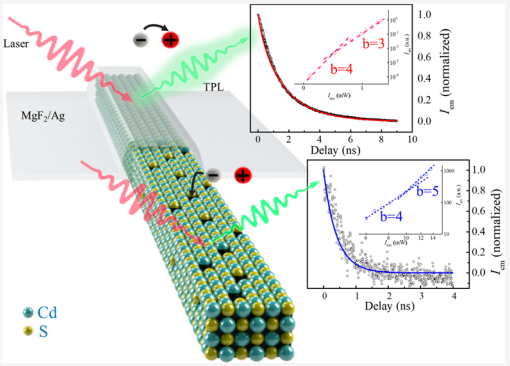

KEYWORDS: *free carrier dynamics, surface defect passivation, two-photon luminescence enhancement, CdS hybrids*

Over the past two decades, quasi one-dimensional (1-D) semiconductor nanostructures, such as nanowires and nanobelts, have been intensively studied.[1−7] These nanostructures demonstrate excellent optical and electric properties compared with those bulk counterparts.[8−11] However, due to large surface-to-volume ratios of nanostructures, surface defects, such as element vacancies and interstitials in the surface, are the dominant defect states in the nanostructure with good crystallinity. For example, since the loss rate of sulfur (S) in traditional CdS structures is much larger than that of cadmium (Cd; S is easily escaped at the temperature as low as 100 °C),[7] a surface depletion layer can be easily created on the surface of the nanostructure due to S vacancies.[12,13] As a result, it induces a localized trap level in the band gap and captures the electrons, leading to fluorescence quenching due to nonradiative electron−hole recombination. Specifically, free carriers can be significantly trapped by S vacancies due to a long diffusion length (~650 nm at room temperature) in CdS NWs, resulting in a fast nonradiative recombination channel (even several times faster than radiative recombination).[14,15] Thus, surface defects significantly degrade the optoelectronic performance of nanostructures.

As previously reported, many studies have been devoted to reducing surface defects.[16−19] In particular, surface passivation, which can eliminate the effects of surface traps formed by dangling bonds and adsorbed species on nanowire surfaces, is widely used for nanodevices fabrication to improve the optoelectronic performance. Usually, the materials with larger band gaps (in comparison with that of the core material) are chosen for the surface passivation layer for confining the electrons and holes efficiently.[20] For example, SiO_2,[21,22] Al_2O_3,[10,23] and poly(methyl methacrylate) (PMMA)[24] are used to passivate the CdS nanomaterial. In addition, halogen elements can effectively passivate the chalcogen vacancies of CdS,[25] ZnO, and the two-dimensional transition metal dichalcogenide (2D-TMD) materials.[27,28] According to the previous works, 1−2 orders of magnitude of fluorescence enhancement can be achieved by surface passivation. Surface passivation can be directly characterized by transmission electron microscopy (TEM) and scanning electron microscopy (SEM),[29] while it can also be qualitatively indicated by fluorescence and surface Raman spectra. However, there is still the lack of an all-optical method to quantitatively characterize

Received: April 16, 2020
Published: October 30, 2020

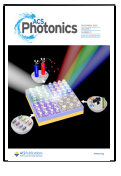

https://dx.doi.org/10.1021/acsphotonics.0c00615
ACS Photonics 2020, 7, 2987−2994

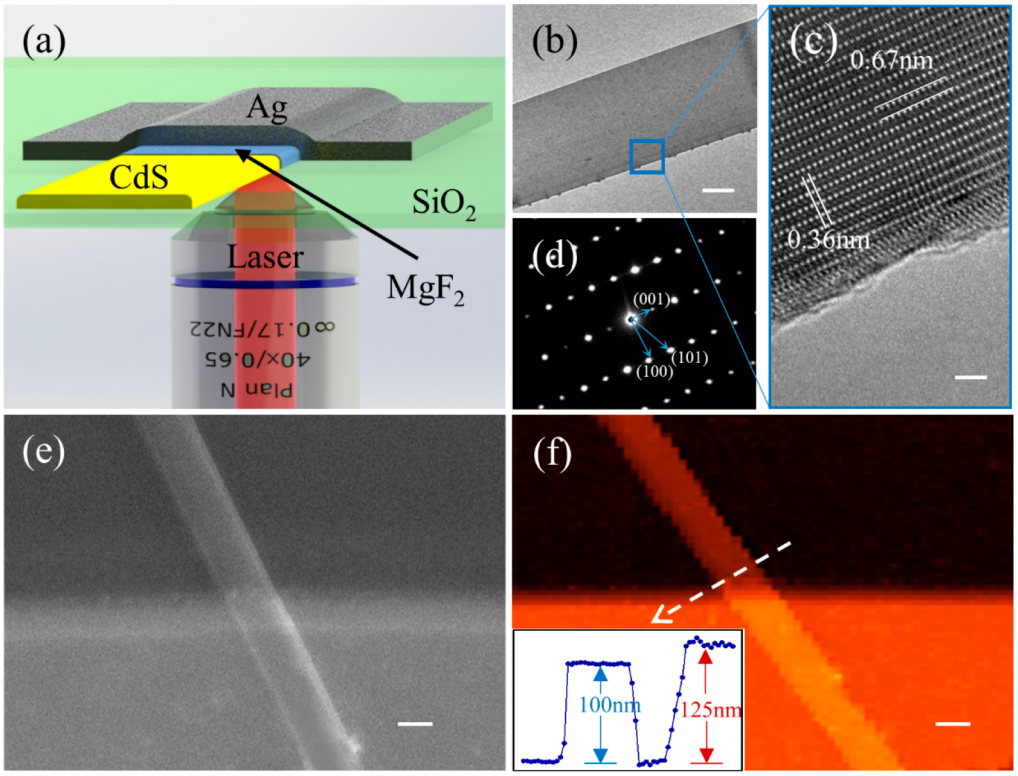

Figure 1. (a) Schematic of a CdS nanobelt and half part is covered by a MgF_2/Ag film. Laser is focused on the CdS nanobelt through the SiO_2 substrate. (b) TEM image of a CdS nanobelt. (c, d) Corresponding HRTEM images (c) and the selected area electron diffraction (SAED) pattern (d) of the CdS nanobelt. Scale bars are 0.2 μm (b) and 2 nm (c), respectively. (e) SEM image of the hybrid nanostructure, where a part of the CdS nanobelt is covered by a MgF_2/Ag film, and the remaining part is bare. Scale bar is 3 μm. (f) Corresponding AFM image of the hybrid structure, where the scale bar is 3 μm. Inset of (f): Cross-sectional profile extracted from the white line in (f), showing the thickness of the CdS nanobelt (~100 nm) and MgF_2/Ag film (~125 nm).

the passivated defect density in real time, which is important to evaluate the optical property of materials.

In this paper, we experimentally demonstrate a 230× enhancement of QY under a two-photon excitation in a single CdS/MgF_2/Ag hybrid nanobelt. A single CdS nanobelt is half covered by the MgF_2/Ag coating,[30] which allows a direct comparison between the TPL properties from the same CdS nanobelt with and without MgF_2/Ag coating. Specifically, the power-dependent TPL and TRPL measurements are performed, which is further quantitatively analyzed by the free carrier dynamic model. It indicates that the surface defect density is reduced from $(3.7 \pm 0.9) \times 10^{19}$ cm^{-3} (bare) to $(3.9 \pm 0.6) \times 10^{18}$ cm^{-3} (hybrid CdS nanobelt) due to the surface passivation, while the radiative recombination rate is increased from $(1.7 \pm 0.2) \times 10^{-11}$ cm^3 s^{-1} (bare) to $(7.1 \pm 1.3) \times 10^{-11}$ cm^3 s^{-1} (hybrid CdS nanobelt) due to the Purcell effect. Furthermore, combined with the enhancement of the local-field at the excitation wavelength (6.3×) and the signal collection efficiency (1.42×), a large TPL enhancement of about 1800× is achieved in experiment. The parametrized dynamic model enables a numerical characterization on surface passivation, providing useful information in high performance nanodevice design.

Figure 1a presents a schematic of the CdS/MgF_2/Ag hybrid nanobelt. A single CdS nanobelt is dispersed on a quartz substrate, half of which is capped by a 10 nm MgF_2 and 115 nm Ag film (see Methods for details). Figure 1b shows the TEM image of a single CdS nanobelt grown by chemical vapor deposition (CVD) method.[31] Figure 1c presents the high-resolution (HR) TEM image of the area indicated by a square shown in Figure 1b. It shows two clear lattice spacings of 0.36 and 0.67 nm, corresponding to [100] and [001] lattice plane of hexagonal CdS, respectively. It reveals that the CdS nanobelts are grown along [100] direction. The corresponding selected area electron diffraction (SAED) pattern is shown in Figure 1d, which suggests the good crystalline quality of the samples. Figure 1e shows a typical SEM image of the hybrid nanobelt, and the corresponding atom force microscope (AFM) image is shown in Figure 1f. The cross-section profile in the inset indicates that the thicknesses of the CdS nanobelt and the MgF_2/Ag film are 100 and 125 nm, respectively. The width of the CdS nanobelt is 2.9 μm, which agrees with the SEM measurement in Figure 1e.

For a clear determination of the TPL enhancement in the CdS/MgF_2/Ag hybrid nanobelt, Figure 2a shows the TPL scanning image for the same area in the sample shown in Figure 1e,f (see Methods for experimental details). It can be seen clearly that the TPL intensity from the CdS/MgF_2/Ag hybrid nanobelt (~6.3×10^{-1}) is significantly larger than that from the bare CdS nanobelt (~3.5×10^{-4}). Figure 2b indicates the TPL spectra of CdS with (red circle) and without (blue circle) MaF_2/Ag coating. Obviously, the TPL intensity from the hybrid nanobelt (red curve) is significantly stronger than that from the bare part (blue curve). Note that the TPL spectrum from the bare CdS nanobelt has been magnified by 100×. It indicates that about 1800× TPL enhancement is achieved (see SI for an enlarged spectra). Moreover, both of the TPL spectra from the two parts of the nanobelt is centered

https://dx.doi.org/10.1021/acsphotonics.0c00615
ACS Photonics 2020, 7, 2987−2994

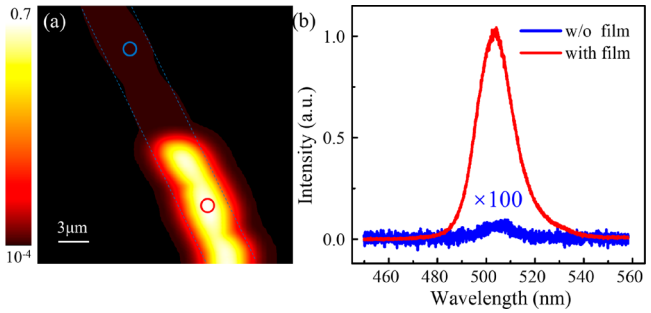

Figure 2. (a) TPL scanning image of CdS nanobelt, the same area of Figure 1e,f. TPL intensity of the CdS/MgF_2/Ag hybrid part is much stronger than the bare part. (b) TPL spectra of the CdS nanobelt with MgF_2/Ag covered (red curve) and without covered (blue cure, multiplied by 100). Both of the peaks are centered at 503 nm.

at 503 nm, which is corresponding to the band-edge emission of the CdS nanobelt (at 2.46 eV).[32] The full width at half-maximum (fwhm) of both curves are the same (20 nm), which also confirms that both TPL signals are band-edge emission. At room temperature, the LO-phonon energy ($\hbar\omega_{LO}$ = 35 meV) is larger than the exciton binding energy (~28 meV), though the binding energy is comparable to thermal energy ($k_BT \sim 25$ meV).[14,33,34] Therefore, free carriers dominate the band-edge emission as excitons are dissociated immediately after generation.

In order to analyze the mechanism of TPL enhancement, the carrier recombination processes in CdS nanobelts are studied by a time-resolved photoluminescence (TRPL) measurement. The hollow dots in Figure 3a,b show the measured TRPL in the bare and the hybrid nanobelt, respectively. A femtosecond laser at 800 nm is used as a pumping source, and the PL decay is monitored at 2.46 eV (503 nm). A dynamic model is developed to analyze the free carrier recombination processes under two-photon absorption (TPA), as shown in Figure 3c. The TRPL decay data of bare and hybrid nanobelts are well fitted, as shown in Figure 3a and b (solid curves), respectively. Specifically, electrons are excited from the valence band to the conduction band through TPA, indicated by path 1 in Figure 3c. The subsequent relaxation process is the thermal process assisted by phonons, which takes a very short time (~ps) and can be ignored in this model. Then the thermalized electrons in the conduction band will radiatively combine with the holes in the valence band (path 2). Meanwhile, they probably move to the surface of the CdS nanobelt and are trapped by the defects due to the large diffusion length (~650 nm),[14,15] and then they recombine nonradiatively (through paths 3 and 4). Since the size of the CdS nanobelts is much larger than the Bohr radius (~2.8 nm), there is no quantum confinement effect in the CdS nanobelts.[35] Note that the Auger process is ignored due to low electron concentration excited by the TPA process. The following differential equations are used to describe the electron and hole concentrations in the CdS nanobelts' conduction and valence band:[36]

$$\frac{dn}{dt} = G - \eta_e \cdot k_r \cdot n \cdot p - k_t(N_e - n_t)n \quad (1)$$

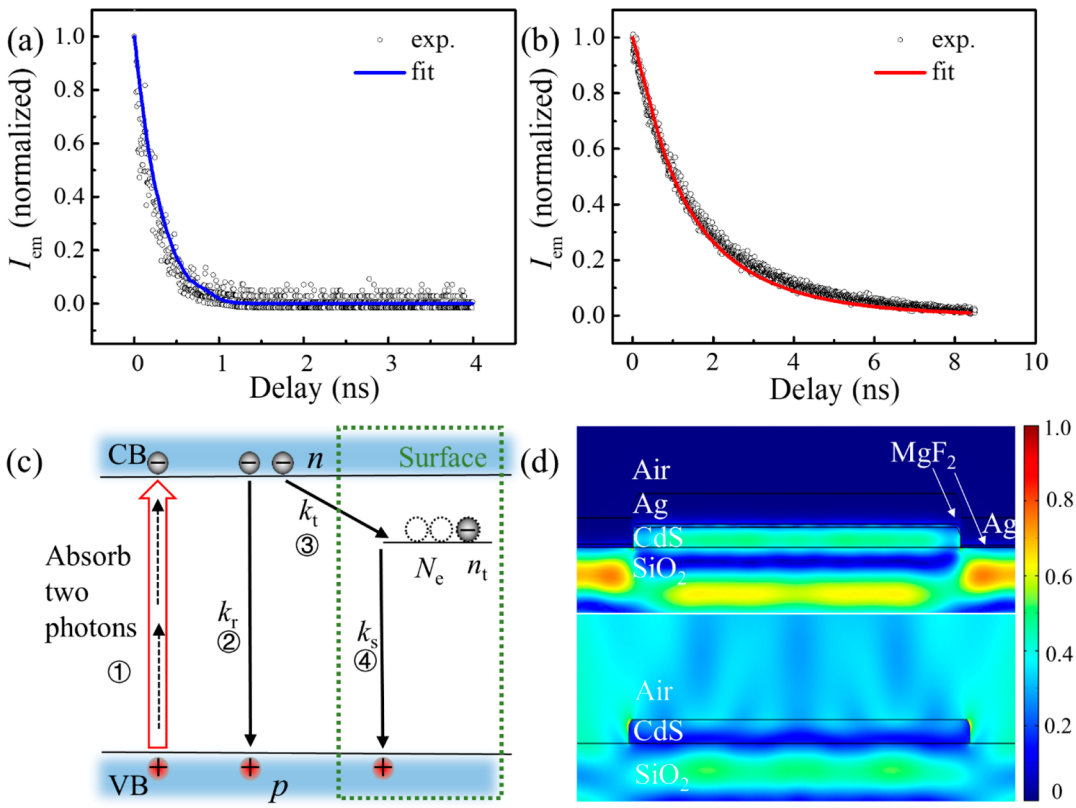

Figure 3. (a, b) Radiative decays of CdS nanobelt without coating (a) and with MgF_2/Ag film coating (b). Hollow dots indicate experimental data and solid curves indicate theoretical fits. (c) Illustration of the model of the TPA and exciton recombination processes in CdS nanobelts. (d) Calculated distribution patterns of the electric-field intensity ($|E_{exc}|$) of the pumping laser in the cross section of the samples (with (upper) and without (lower) MgF_2/Ag film).

https://dx.doi.org/10.1021/acsphotonics.0c00615
ACS Photonics 2020, 7, 2987−2994

Table 1. Theoretical Fitting Values of N_e, k_r, k_t, and k_s in the Bare Nanobelt and Hybrid Structure

	N_e (cm^{-3})	k_r (cm^3/s)	k_t (cm^3/s)	k_s (cm^3/s)
$CdS/MgF_2/Ag$ hybrid	$(3.9 \pm 0.6) \times 10^{18}$	$(7.1 \pm 1.3) \times 10^{-11}$	$(2 \pm 0.2) \times 10^{-10}$	$(1 \pm 0.3) \times 10^{-11}$
bare CdS nanobelt	$(3.7 \pm 0.9) \times 10^{19}$	$(1.7 \pm 0.2) \times 10^{-11}$	$(2.1 \pm 0.3) \times 10^{-10}$	$(1 \pm 0.3) \times 10^{-11}$

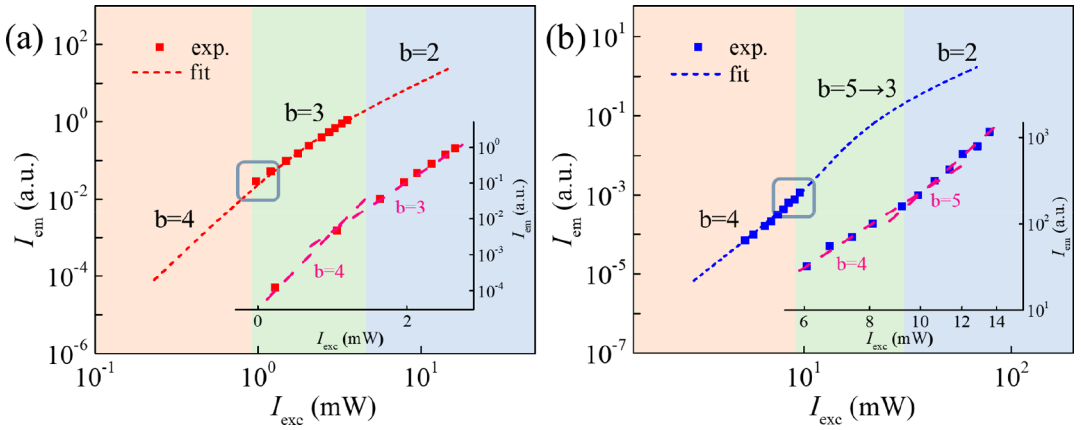

Figure 4. Power-dependent TPL intensity for the MgF_2/Ag covered (a) and the same bare (b) CdS nanobelt. Square dots indicate experimental data and dash lines indicate theoretical fits. The insets of (a) and (b) are the enlargement of the data in the gray squares, which show a transition of the coefficient b from 4 to 3 or 5, respectively.

$$\frac{dn_t}{dt} = k_t(N_e - n_t)n - k_s \cdot n_t \cdot p \quad (2)$$

$$\frac{dp}{dt} = G - \eta_e \cdot k_r \cdot n \cdot p - k_s \cdot n_t \cdot p \quad (3)$$

where n (p) is the electron (hole) concentration in the conduction (valence) band and n_t is trapped electron concentration. N_e is the concentration of surface defects. η_e is a dimensionless photon extraction efficiency (assumed to be unity due to the subwavelength thicknesses of the investigated nanobelts).[37] k_r, k_t, and k_s are the constants of the bimolecular radiative recombination rate, electron trapping (nonradiative) rate, and trapped electron (nonradiative) recombination rate, respectively. G represents the electron or hole generation rate, depending on experimental excitation intensities through $G = \beta I_{exc}^2$, where β is the TPA coefficient ($\beta \approx 10$ cm/GW in CdS at 800 nm),[38,39] and the excitation intensity (I_{exc}) is ~26 GW/cm^2 for the bare CdS nanobelt. Furthermore, the finite-element simulation demonstrates the average electric-field intensity (E_{exc}) in CdS nanobelt in hybrid structure is 1.59× stronger than that in the bare nanobelt, shown in Figure 3d (see SI for details). This is due to the localization of the electromagnetic field by the metal nanocavity, which is composed of the CdS nanobelt and the MgF_2/Ag film.[40,41] Therefore, the electron generation rate ($G = \beta I_2^{exc} = \beta |E_{exc}|^4$) is enhanced 6.3× in the hybrid structure.

The equations can be numerically solved by the Runge–Kutta algorithm, with the initial values of n and p estimated from the electron or hole generation rate G. The other four parameters (N_e, k_r, k_t, k_s) are obtained by fitting the TRPL data through the equation $I_{em}(t) = \eta_e \cdot k_r \cdot n(t) \cdot p(t)$. The fitting curve at different excitation intensities can be found in Figure S1, and the fitted results are listed in Table 1 (more details are shown in the SI).

Figure S1 shows that these four parameters are consistent with the TRPL data at different powers, and the fitted values in the bare CdS nanobelt are consistent with the previous works.[15,42−45] In addition, the errors of the four parameters are estimated through multiple measurements (see SI for more details). According to Table 1, the defect density in the CdS/MgF_2/Ag hybrid is decreased from $(3.7 \pm 1.9) \times 10^{19}$ cm^{-3} to $(3.9 \pm 0.6) \times 10^{18}$ cm^{-3} in comparison with the bare CdS nanobelt, indicating that the surface defects of the CdS nanobelt are passivated effectively. In CdS, the S element more easily escaped due to a lower boiling point than that of Cd,[12,13] forming a deep level (1.8 eV) of the traps on the surface,[46] and it is well-known that the fluorine (F) element can fill the S vacancy on the surface and repair the energy band, so that coating MgF_2 is an important method to passivate the CdS nanobelt.[25,26] Furthermore, in order to directly validate the passivation of MgF_2, TRPL of CdS nanobelt covered by 10 nm MgF_2 is measured. The results demonstrate that the defect density in CdS/MgF_2 is reduced to 3.5×10^{18} cm^{-3}, which is similar to that in the CdS/MgF_2/Ag hybrid (see SI for more details). Therefore, it indicates that the MgF_2 layer can effectively passivate the surface defects on the CdS nanobelts.

Meanwhile, MgF_2, as an isolation layer, combine with Ag to form a nanocavity. The increase of radiative recombination rate (k_r) in the hybrid structure is ascribed to the Purcell effect due to the nanocavity. Since the photon state density in the nanocavity is increased remarkably, the interaction between photons and electrons is enhanced, and then it results in the increase of the radiation recombination rate. The Purcell factor in cavity is calculated to be 4.2, through $\frac{k_r'}{k_r}$, where k_r' and k_r are the radiative recombination rate in cavity and bare CdS nanobelt, respectively.[9] In addition, because the Purcell effect is related to the quality of the cavity, we have systematically studied the relationship between Purcell factor and thickness (see SI for more details).

According to the kinetic model, the carrier number of radiative recombination (N_r) and nonradiative recombination (N_{nr}) are obtained and QY is calculated through $QY = \frac{N_r}{2(N_{nr} + N_r)}$,[47] where constant 2 is originated from the two-photon absorption. The QY of the bare CdS nanobelt and the hybrid structure is calculated to be 0.05% and 11.5%,

https://dx.doi.org/10.1021/acsphotonics.0c00615
ACS Photonics 2020, 7, 2987−2994

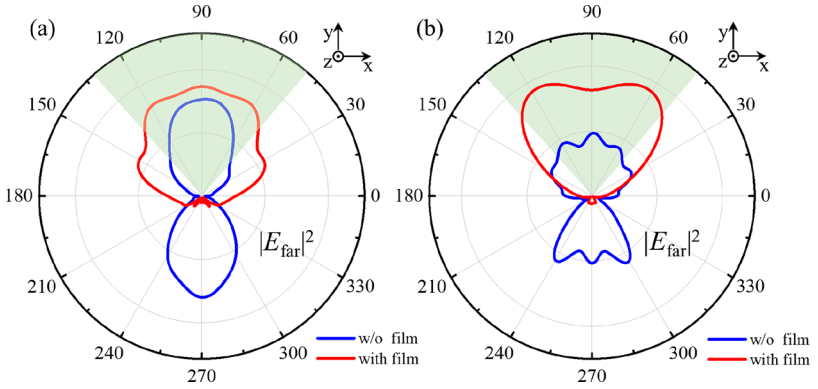

Figure 5. Polar plots of the calculated far-field intensity $|E_{far}|^2$ distribution of the TPL signal. The nanobelt is placed along the *z*-axis. The TPL signals are *z*- (a) and *x*-polarizations (b), respectively. The green area shows the collection cone of the objective.

respectively. Therefore, a 230× QY enhancement is observed in the CdS/MgF_2/Ag hybrids. It is noting that the QY is power-dependent, because the trap-related nonradiative recombination process is gradually saturated, as the excitation power increases. Thus, the proportion of the radiative recombination gradually increases, as shown in Figure S7. Moreover, the QY is very low in the bare nanobelt, because of high defect density, while the QY is high in the hybrid structure due to low defect density and saturation of the nonradiative recombination.

Figure 4 shows the measured TPL intensity as a function of the pumping power for the bare and hybrid CdS nanobelt. The emission intensities are increased in a power-law fashion: $I_{em} \propto I_{exc}^b$, where power-law coefficient, *b*, reflects the underlying carrier recombination processes.[36] Since the TPA is proportional to the quadratic of the excitation intensity, quadratic growth of I_{em} (i.e., $I_{em} \propto I_{exc}^b$, $b = 2$) is reasonable in the case of TPL. However, the experiment data (the hollow dots) and theoretical fitting using the dynamic model (the dash lines; shown in Figure 4) indicate that the practical power-law coefficients (*b*) is ∼4 and ∼3 for bare CdS nanobelt and capped part, respectively. In general, when the trapping process dominates the recombination processes, the growth exponent *b* will be 4, and the saturation of the trap-related recombination channel reduces the coefficient *b* to 2 (see SI for details). Furthermore, competition between intrinsic and trap-related recombination results in the variation of *b* from 4 to 2. Besides, TPA saturation can also lead to the decrease of the *b*.[48] For investigating the effect of TPA saturation on the power-law coefficients *b*, the TPA saturation model is introduced in the dynamic model. The results show that the saturation power of the nanobelt is ranging from 190 GW/cm^2 to infinity and the saturation effect has little influence on coefficient *b* and can be ignored (see SI for details).[39,49,50] According to our experimental data, the processes of *b* transition from 4 to 2 at different defect density are different. Using our model and the parameters in Table 1, the experimental data are well fitted without TPA saturation. In Figure 4a, experimental data and theoretical fitting show that the variation of *b* value in hybrid nanobelt is direct (4 → 3 → 2) due to the low surface defect concentration. In contrast, Figure 4b shows that the coefficient *b* in the bare CdS nanobelt first increases to 5 and subsequently falls to 2 due to the higher surface defect density than that in hybrid structure. Therefore, the power-dependent measurement provides an insight into the proportion of trap-related recombination, and the dynamic model can accurately characterize the defect concentration in the nanobelt.

In addition, the TPL signals are collected by an objective with a collection cone angle of about 80 degrees (40×, 0.65 NA). Therefore, a certain amount of the TPL signal is not collected due to the large divergence.[51] In a hybrid structure there is a nanocavity formed by MgF_2/Ag film that can efficiently gather the TPL signals, leading to the signal collection efficiency improvement. We used commercial finite element simulation software to analyze changes of emission angle and the collection efficiency in hybrid structures. For simplifying the calculation, a point electric dipole at 376 THz (503 nm) was placed in the center of a CdS nanobelt to act as a TPL emission source,[52] whose polarization is in the substrate plane and parallel or perpendicular to long axis of CdS nanobelt (see SI for details). Figure 5a,b shows the typical cross-section of far-field radiation of the MgF_2/Ag film-covered and the bare CdS nanobelt, whose polarization is parallel or perpendicular to long-axis of CdS nanobelt. Obviously, the TPL signals radiated from the hybrid structure are concentrated. The collection efficiency is determined by the ratio between the far-field intensity ($|E_{far}|^2$) within the collection cone and the total far-field intensity. By comparing the collection efficiency of the structure with and without MgF_2/Ag film coating, the enhancements of the TPL collection efficiencies are obtained. Additionally, the angular dependence of emission shown in Figure 5 is attributed to the surrounding dielectric materials rather than the dipole oscillation direction, which can also lead to the phenomenon.[53,54] The enhancements are calculated to be 1.4-fold for *z*-polarization (Figure 5a) and 1.5-fold for *x*-polarization (Figure 5b). In order to further confirm the change of the signal collection, the polarization of the TPL was measured, as shown in Figure S9. The numerical fitting results show that the intensity of TPL polarized along *z*-axis is three times large than that polarized along *x*-axis. Therefore, collection efficiency is enhanced by 1.42×.

Considering the 6.3× local-field enhancement, 1.42× collection efficiency, and 230× QY enhancement, the total enhancement factor of the TPL in hybrid structure is calculated to be 2057×, which is similar to the experiment data (1800×). It is noting that the TPL is compared at the different parts of the same CdS nanobelt, thus, the transition dipole moments and related TPA cross sections have no influence on the TPL enhancement.[49,55] In addition, due to the large enhancement of TPL and low divergence angle, this

https://dx.doi.org/10.1021/acsphotonics.0c00615
ACS Photonics 2020, 7, 2987−2994

hybrid nanobelts is quite suitable for autocorrelation measurement.[56] Furthermore, the MgF_2/Ag layer not only can be used as a spacer layer and an electrode, but also can passivate the CdS nanobelt to improve the luminous efficiency. Hence, it can be widely used in light-emitting diodes and nanolasers.

In conclusion, we experimentally demonstrate a giant TPL enhancement of about 1800× in the CdS/MgF_2/Ag hybrid structure, which is obtained by direct comparison between the same CdS nanobelt with and without MgF_2/Ag coating. By analyzing TRPL and the power-dependent TPL results with a free carrier dynamic model, the surface defect density and the carrier recombination rates in the bare and hybrid CdS nanobelt are obtained. It indicates that the surface defect concentration is decreased from $(3.7 \pm 0.9) \times 10^{19}$ cm^{-3} (in bare) to $(3.9 \pm 0.6) \times 10^{18}$ cm^{-3} (in CdS hybrid nanobelt) due to the surface passivation, while the radiative recombination rate is increased from $(1.7 \pm 0.2) \times 10^{-11}$ cm^3 s^{-1} (in bare) to $(7.1 \pm 1.3) \times 10^{-11}$ cm^3 s^{-1} (in CdS hybrid) due to the Purcell effect. Totally, a 230× QY enhancement is achieved in a hybrid nanobelt, which is increased from 0.05% (in bare) to 11.5% (in CdS hybrid). Furthermore, the finite element simulation indicates the hybrid structure can support the local-field enhancement (6.3×) at the excitation wavelength and gather the emitted TPL signal for collection, leading to an additional enhancement of ∼8.9×. Our work provides an all-optical method for characterizing the surface passivation quantitatively, which has potential applications in the high-performance in optoelectronic devices, such as photovoltaics and photodetectors.

METHODS

CdS Nanobelt Synthesis and Characterizations. The CdS nanobelts used in the experiments were synthesized by the CVD method described previously.[31] The widths of the CdS nanobelt are about 1−4 μm, and the thicknesses are about 60−130 nm. SEM (Nova NanoSEM 450), HRTEM (Titan G2 60−300 Probe Cs Corrector HRSTEM), and AFM (Veeco NanoScope MultiMode) were used to assess the morphology and the crystalline quality of the CdS nanobelts.

CdS/MgF_2/Ag Film Structure Fabrication. A lift-off process was used to fabricate the MgF_2/Ag film covering the CdS nanobelts.[30] The detailed steps are as follows: First, CdS nanobelts are dispersed from the grown substrate (silicon substrate) into ethanol solution and then deposited onto a quartz substrate; Second, the quartz substrate with CdS nanobelts goes through standard photolithography treatments, namely, photoresist coating, exposure, and developing; Third, a MgF_2/Ag film with a thickness of about 10 nm MgF_2 and 115 nm Ag is deposited onto the quartz substrate by electron beam evaporation; Finally, after removing the remaining photoresist with acetone, the MgF_2/Ag film covered on the photoresist will be removed automatically and the designed microstructure is left on the substrate.

Optical Measurements. Optical measurements of the individual CdS nanobelts were carried out at room temperature using an inverted microscope (IX73, Olympus) configured with a two-dimension motorized stage (BIOS-L101T-S, SIGMAKOKI). The laser (produced by Vitara Coherent, 800 nm, 30 fs, and 80 MHz) is focused onto the CdS nanobelt through a quartz substrate by a 40× objective (Olympus, 0.65 NA) for exciting TPL. The diameter of the focused spot is about 2 μm. The TPL was spectrally resolved with a monochromator (Andor, SR193i) and measured by a thermoelectric-cooled charge CCD (Andor ivac316). Additionally, the intensity of the TPL is measured by a photomultiplier (PMT, Hamamatsu H7827) after removing the pumping laser with a short-pass filter (Semrock, SP 720 nm). A time-correlated single-photon counting (TCSPC) system (Picoquant, Picoharp 300) was equipped behind the spectrometer for time-resolved photoluminescence (TRPL) measurement (the model of the detector is PDM (MPD company)).

ASSOCIATED CONTENT

Supporting Information

The Supporting Information is available free of charge at https://pubs.acs.org/doi/10.1021/acsphotonics.0c00615.

The dynamic model of the free carriers for TRPL and $I_{em}-I_{exc}$ fitting; The finite element simulation; The passivation effect in CdS/MgF_2; The Purcell effect in hybrids of different MgF_2 thicknesses; The power-dependence QY; The TPA saturation model; The measurement of the TPL polarization; The estimation of uncertainty; Results of the 400 nm laser excitation (PDF)

AUTHOR INFORMATION

Corresponding Authors

Kai Wang − *Wuhan National Laboratory for Optoelectronics and School of Physics, Huazhong University of Science and Technology, Wuhan 430074, China;* orcid.org/0000-0003-2122-1294; Email: kale_wong@hust.edu.cn

Peixiang Lu − *Wuhan National Laboratory for Optoelectronics and School of Physics, Huazhong University of Science and Technology, Wuhan 430074, China; Hubei Key Laboratory of Optical Information and Pattern Recognition, Wuhan Institute of Technology, Wuhan 430205, China; CAS Center for Excellence in Ultra-Intense Laser Science, Shanghai 201800, China*; Email: lupeixiang@hust.edu.cn

Authors

Xiangyuan Xing − *Wuhan National Laboratory for Optoelectronics and School of Physics, Huazhong University of Science and Technology, Wuhan 430074, China*

Xiaobo Han − *Hubei Key Laboratory of Optical Information and Pattern Recognition, Wuhan Institute of Technology, Wuhan 430205, China*

Shuhang Qian − *Wuhan National Laboratory for Optoelectronics and School of Physics, Huazhong University of Science and Technology, Wuhan 430074, China*

Kun Wang − *Wuhan National Laboratory for Optoelectronics and School of Physics, Huazhong University of Science and Technology, Wuhan 430074, China*

Hua Long − *Wuhan National Laboratory for Optoelectronics and School of Physics, Huazhong University of Science and Technology, Wuhan 430074, China*

Bing Wang − *Wuhan National Laboratory for Optoelectronics and School of Physics, Huazhong University of Science and Technology, Wuhan 430074, China*

Complete contact information is available at: https://pubs.acs.org/10.1021/acsphotonics.0c00615

Notes

The authors declare no competing financial interest.

https://dx.doi.org/10.1021/acsphotonics.0c00615
ACS Photonics 2020, 7, 2987−2994

■ ACKNOWLEDGMENTS

This work was supported by the National Natural Science Foundation of China (Nos. 11774115, 91850113, and 11904271) and the 973 Programs under Grant 2014CB921301. A special thanks to the Analytical and Testing Center of HUST for the use of their facilities. Thanks to the facility support of the Center of Micro-Fabrication and Characterization (CMFC) and the Center of Nanoscale Characterization and Devices (CNCD), WNLO of HUST.

■ REFERENCES

(1) Utama, M. I. B.; Zhang, J.; Chen, R.; Xu, X.; Li, D.; Sun, H.; Xiong, Q. Synthesis and optical properties of II−VI 1D nanostructures. *Nanoscale* **2012**, *4* (5), 1422−1435.
(2) Jie, J.; Zhang, W.; Bello, I.; Lee, C.-S.; Lee, S.-T. One-dimensional II−VI nanostructures: Synthesis, properties and optoelectronic applications. *Nano Today* **2010**, *5* (4), 313−336.
(3) Xia, Y.; Yang, P.; Sun, Y.; Wu, Y.; Mayers, B.; Gates, B.; Yin, Y.; Kim, F.; Yan, H. One-Dimensional Nanostructures: Synthesis, Characterization, and Applications. *Adv. Mater.* **2003**, *15* (5), 353−389.
(4) Shi, Y.; Ma, Z.; Zhao, D.; Chen, Y.; Cao, Y.; Wang, K.; Xiao, G.; Zou, B. Pressure-Induced Emission (PIE) of One-Dimensional Organic Tin Bromide Perovskites. *J. Am. Chem. Soc.* **2019**, *141* (16), 6504−6508.
(5) Cunningham, P. D.; Boercker, J. E.; Foos, E. E.; Lumb, M. P.; Smith, A. R.; Tischler, J. G.; Melinger, J. S. Enhanced Multiple Exciton Generation in Quasi-One-Dimensional Semiconductors. *Nano Lett.* **2011**, *11* (8), 3476−3481.
(6) Song, B.; Zhong, Y.; Wu, S.; Chu, B.; Su, Y.; He, Y. One-Dimensional Fluorescent Silicon Nanorods Featuring Ultrahigh Photostability, Favorable Biocompatibility, and Excitation Wavelength-Dependent Emission Spectra. *J. Am. Chem. Soc.* **2016**, *138* (14), 4824−4831.
(7) Jassim, N. M.; Wang, K.; Han, X.; Long, H.; Wang, B.; Lu, P. Plasmon assisted enhanced second-harmonic generation in single hybrid Au/ZnS nanowires. *Opt. Mater.* **2017**, *64*, 257−261.
(8) Liu, X.; Zhang, Q.; Chong, W. K.; Yip, J. N.; Wen, X.; Li, Z.; Wei, F.; Yu, G.; Xiong, Q.; Sum, T. C. Cooperative Enhancement of Second-Harmonic Generation from a Single CdS Nanobelt-Hybrid Plasmonic Structure. *ACS Nano* **2015**, *9* (5), 5018−5026.
(9) Oulton, R. F.; Sorger, V. J.; Zentgraf, T.; Ma, R. M.; Gladden, C.; Dai, L.; Bartal, G.; Zhang, X. Plasmon lasers at deep subwavelength scale. *Nature* **2009**, *461* (7264), 629−632.
(10) Duan, X.; Huang, Y.; Agarwal, R.; Lieber, C. M. Single-nanowire electrically driven lasers. *Nature* **2003**, *421* (6920), 241−245.
(11) Zhao, W.; Wang, K.; Hong, X.; Wang, B.; Han, X.; Long, H.; Wang, B.; Lu, P. Chirality-selected second-harmonic holography with phase and binary amplitude manipulation. *Nanoscale* **2020**, *12* (25), 13330−13337.
(12) Christmann, M. H.; Dierssen, G. H.; Salmon, O. N.; Taylor, A. L.; Thom, W. H. Native defect changes in cds single crystal platelets induced by vacuum heat treatments at temperatures up to 600°C. *J. Phys. Chem. Solids* **1975**, *36* (12), 1371−1374.
(13) Xiao, Q.; Xiao, C. Surface-defect-states photoluminescence in CdS nanocrystals prepared by one-step aqueous synthesis method. *Appl. Surf. Sci.* **2009**, *255* (16), 7111−7114.
(14) Weber, C.; Becker, U.; Renner, R.; Klingshirn, C. Measurement of the diffusion-length of carriers and excitons in CdS using laser-induced transient gratings. *Z. Phys. B: Condens. Matter* **1988**, *72* (3), 379−384.
(15) Liu, X.; Zhang, Q.; Xing, G.; Xiong, Q.; Sum, T. C. Size-Dependent Exciton Recombination Dynamics in Single CdS Nanowires beyond the Quantum Confinement Regime. *J. Phys. Chem. C* **2013**, *117* (20), 10716−10722.
(16) Lu, D.; Zhang, Y.; Lai, M. L.; Lee, A.; Xie, C. L.; Lin, J.; Lei, T.; Lin, Z. N.; Kley, C. S.; Huang, J. M.; Rabani, E.; Yang, P. D. Giant Light-Emission Enhancement in Lead Halide Perovskites by Surface Oxygen Passivation. *Nano Lett.* **2018**, *18* (11), 6967−6973.
(17) van Vugt, L. K.; Veen, S. J.; Bakkers, E. P. A. M.; Roest, A. L.; Vanmaekelbergh, D. Increase of the Photoluminescence Intensity of InP Nanowires by Photoassisted Surface Passivation. *J. Am. Chem. Soc.* **2005**, *127* (35), 12357−12362.
(18) Sun, M. H.; Joyce, H. J.; Gao, Q.; Tan, H. H.; Jagadish, C.; Ning, C. Z. Removal of Surface States and Recovery of Band-Edge Emission in InAs Nanowires through Surface Passivation. *Nano Lett.* **2012**, *12* (7), 3378−3384.
(19) Al-Nafiey, A.; Sieber, B.; Gelloz, B.; Addad, A.; Moreau, M.; Barjon, J.; Girleanu, M.; Ersen, O.; Boukherroub, R. Enhanced Ultraviolet Luminescence of ZnO Nanorods Treated by High-Pressure Water Vapor Annealing (HWA). *J. Phys. Chem. C* **2016**, *120* (8), 4571−4580.
(20) Shi, L.; Xu, Y.; Hark, S.; Liu, Y.; Wang, S.; Peng, L.-m.; Wong, K.; Li, Q. Optical and Electrical Performance of SnO_2Capped ZnO Nanowire Arrays. *Nano Lett.* **2007**, *7* (12), 3559−3563.
(21) van Vugt, L. K.; Piccione, B.; Cho, C.-H.; Aspetti, C.; Wirshba, A. D.; Agarwal, R. Variable Temperature Spectroscopy of As-Grown and Passivated CdS Nanowire Optical Waveguide Cavities. *J. Phys. Chem. A* **2011**, *115* (16), 3827−3833.
(22) Cho, C. H.; Aspetti, C. O.; Turk, M. E.; Kikkawa, J. M.; Nam, S. W.; Agarwal, R. Tailoring hot-exciton emission and lifetimes in semiconducting nanowires via whispering-gallery nanocavity plasmons. *Nat. Mater.* **2011**, *10* (9), 669−675.
(23) Ahn, C. H.; Kang, W. J.; Kim, Y. K.; Yun, M. G.; Cho, H. K. Highly Repeatable and Recoverable Phototransistors Based on Multifunctional Channels of Photoactive CdS, Fast Charge Transporting ZnO, and Chemically Durable Al2O3 Layers. *ACS Appl. Mater. Interfaces* **2016**, *8* (24), 15518−15523.
(24) Li, D.; Zhang, J.; Xiong, Q. Surface Depletion Induced Quantum Confinement in CdS Nanobelts. *ACS Nano* **2012**, *6* (6), 5283−5290.
(25) Zeng, Y.; Xing, H.; Huang, Y.; Lu, A.; Wang, C.; Xu, X.; Wang, J.; Chen, X. Enhanced surface modification engineering (H, F, Cl, Br, and NO_2) of CdS nanowires with and without surface dangling bonds. *J. Appl. Phys.* **2015**, *118* (5), 054305.
(26) Harada, Y.; Hashimoto, S. Enhancement of band-edge photoluminescence of bulk ZnO single crystals coated with alkali halide. *Phys. Rev. B: Condens. Matter Mater. Phys.* **2003**, *68* (4), 045421.
(27) Mastria, R.; Loiudice, A.; Vávra, J.; Nobile, C.; Scarfiello, R.; Cozzoli, P. D.; Sestu, N.; Marongiu, D.; Quochi, F.; Buonsanti, R.; Saba, M.; Calzolari, A.; Rizzo, A. Photoluminescence Emission Induced by Localized States in Halide Passivated Colloidal Two-Dimensional WS_2 Nanoflakes. *ChemRxiv Preprint* **2019**, na.
(28) Han, H.-V.; Lu, A.-Y.; Lu, L.-S.; Huang, J.-K.; Li, H.; Hsu, C.-L.; Lin, Y.-C.; Chiu, M.-H.; Suenaga, K.; Chu, C.-W.; Kuo, H.-C.; Chang, W.-H.; Li, L.-J.; Shi, Y. Photoluminescence Enhancement and Structure Repairing of Monolayer $MoSe_2$ by Hydrohalic Acid Treatment. *ACS Nano* **2016**, *10* (1), 1454−1461.
(29) Amani, M.; Taheri, P.; Addou, R.; Ahn, G. H.; Kiriya, D.; Lien, D.-H.; Ager, J. W.; Wallace, R. M.; Javey, A. Recombination Kinetics and Effects of Superacid Treatment in Sulfur- and Selenium-Based Transition Metal Dichalcogenides. *Nano Lett.* **2016**, *16* (4), 2786−2791.
(30) Hu, H.; Wang, K.; Long, H.; Han, X.; Chen, J.; Wang, B.; Lu, P. Concentrated second-harmonic generation from a single Al-covered ZnS nanobelt. *Laser Photonics Rev.* **2017**, *11* (1), 1600263.
(31) Zhang, L.; Wang, K.; Liu, Z.; Yang, G.; Shen, G.; Lu, P. Two-photon pumped lasing in a single CdS microwire. *Appl. Phys. Lett.* **2013**, *102* (21), 211915.
(32) Xu, X. L.; Zhao, Y. Y.; Sie, E. J.; Lu, Y. H.; Liu, B.; Ekahana, S. A.; Ju, X.; Jiang, Q. K.; Wang, J. B.; Sun, H. D.; Sum, T. C.; Huan, C. H. A.; Feng, Y. P.; Xiong, Q. H. Dynamics of Bound Exciton Complexes in CdS Nanobelts. *ACS Nano* **2011**, *5* (5), 3660−3669.

https://dx.doi.org/10.1021/acsphotonics.0c00615
ACS Photonics 2020, 7, 2987−2994

(33) Woggon, U.; Hild, K.; Gindele, F.; Langbein, W.; Hetterich, M.; Grün, M.; Klingshirn, C. Huge binding energy of localized biexcitons in CdS/ZnS quantum structures. *Phys. Rev. B: Condens. Matter Mater. Phys.* **2000**, *61* (19), 12632−12635.
(34) Liu, X.; Zhang, Q.; Xiong, Q.; Sum, T. C. Tailoring the Lasing Modes in Semiconductor Nanowire Cavities Using Intrinsic Self-Absorption. *Nano Lett.* **2013**, *13* (3), 1080−1085.
(35) Matsuura, D.; Kanemitsu, Y.; Kushida, T.; White, C. W.; Budai, J. D.; Meldrum, A. Photoluminescence Dynamics of CdS Nanocrystals Fabricated by Sequential Ion Implantation. *Jpn. J. Appl. Phys.* **2001**, *40* (Part 1, No.3B), 2092−2094.
(36) Vietmeyer, F.; Frantsuzov, P. A.; Janko, B.; Kuno, M. Carrier recombination dynamics in individual CdSe nanowires. *Phys. Rev. B: Condens. Matter Mater. Phys.* **2011**, *83* (11), na.
(37) Wang, C.; Li, C.-Y.; Hasselbeck, M. P.; Imangholi, B.; Sheik-Bahae, M. Precision, all-optical measurement of external quantum efficiency in semiconductors. *J. Appl. Phys.* **2011**, *109* (9), 093108.
(38) Krauss, T. D.; Wise, F. W. Femtosecond measurement of nonlinear absorption and refraction in CdS, ZnSe, and ZnS. *Appl. Phys. Lett.* **1994**, *65* (14), 1739−1741.
(39) He, J.; Mi, J.; Li, H.; Ji, W. Observation of Interband Two-Photon Absorption Saturation in CdS Nanocrystals. *J. Phys. Chem. B* **2005**, *109* (41), 19184−19187.
(40) Han, X.; Wang, K.; Xing, X.; Wang, M.; Lu, P. Rabi Splitting in a Plasmonic Nanocavity Coupled to a WS_2 Monolayer at Room Temperature. *ACS Photonics* **2018**, *5* (10), 3970−3976.
(41) Chen, J.; Wang, K.; Wu, K.; Qian, L.; Long, H.; Wang, B.; Lu, P. Optimization of metal-enhanced fluorescence by different concentrations of gold-silica core−shell nanoparticles. *Opt. Commun.* **2015**, *349*, 180−184.
(42) Morozov, Y. V.; Draguta, S.; Zhang, S.; Cadranel, A.; Wang, Y.; Janko, B.; Kuno, M. Defect-Mediated CdS Nanobelt Photoluminescence Up-Conversion. *J. Phys. Chem. C* **2017**, *121* (30), 16607−16616.
(43) Sadhu, S.; Saha Chowdhury, P.; Patra, A. Synthesis and time-resolved photoluminescence spectroscopy of capped CdS nanocrystals. *J. Lumin.* **2008**, *128* (7), 1235−1240.
(44) Liu, H. W.; Lu, J. P.; Fan, H. M.; Sow, C. H.; Tang, S. H.; Zhang, X. H. Temperature and composition dependence of photoluminescence dynamics in $CdS_xSe_{1-x}(0 \leq x \leq 1)$ nanobelts. *J. Appl. Phys.* **2012**, *111* (7), 073112.
(45) Sadhu, S.; Patra, A. Relaxation Dynamics of Anisotropic Shaped CdS Nanoparticles. *J. Phys. Chem. C* **2011**, *115* (34), 16867−16872.
(46) Cao, B. L.; Jiang, Y.; Wang, C.; Wang, W. H.; Wang, L. Z.; Niu, M.; Zhang, W. J.; Li, Y. Q.; Lee, S. T. Synthesis and Lasing Properties of Highly Ordered CdS Nanowire Arrays. *Adv. Funct. Mater.* **2007**, *17* (9), 1501−1506.
(47) Draguta, S.; Thakur, S.; Morozov, Y. V.; Wang, Y.; Manser, J. S.; Kamat, P. V.; Kuno, M. Spatially Non-uniform Trap State Densities in Solution-Processed Hybrid Perovskite Thin Films. *J. Phys. Chem. Lett.* **2016**, *7* (4), 715−721.
(48) Achtstein, A. W.; Ballester, A.; Movilla, J. L.; Hennig, J.; Climente, J. I.; Prudnikau, A.; Antanovich, A.; Scott, R.; Artemyev, M. V.; Planelles, J.; Woggon, U. One- and Two-Photon Absorption in CdS Nanodots and Wires: The Role of Dimensionality in the One- and Two-Photon Luminescence Excitation Spectrum. *J. Phys. Chem. C* **2015**, *119* (2), 1260−1267.
(49) Scott, R.; Achtstein, A. W.; Prudnikau, A.; Antanovich, A.; Christodoulou, S.; Moreels, I.; Artemyev, M.; Woggon, U. Two Photon Absorption in II−VI Semiconductors: The Influence of Dimensionality and Size. *Nano Lett.* **2015**, *15* (8), 4985−4992.
(50) Gu, B.; Fan, Y.-X.; Chen, J.; Wang, H.-T.; He, J.; Ji, W. Z-scan theory of two-photon absorption saturation and experimental evidence. *J. Appl. Phys.* **2007**, *102* (8), 083101.
(51) Han, X.; Wang, K.; Persaud, P. D.; Xing, X.; Liu, W.; Long, H.; Li, F.; Wang, B.; Singh, M. R.; Lu, P. Harmonic Resonance Enhanced Second-Harmonic Generation in the Monolayer WS_2−Ag Nanocavity. *ACS Photonics* **2020**, *7* (3), 562−568.
(52) Michetti, P.; La Rocca, G. C. Simulation of J-aggregate microcavity photoluminescence. *Phys. Rev. B: Condens. Matter Mater. Phys.* **2008**, *77* (19), 195301.
(53) Scott, R.; Heckmann, J.; Prudnikau, A. V.; Antanovich, A.; Mikhailov, A.; Owschimikow, N.; Artemyev, M.; Climente, J. I.; Woggon, U.; Grosse, N. B.; Achtstein, A. W. Directed emission of CdSe nanoplatelets originating from strongly anisotropic 2D electronic structure. *Nat. Nanotechnol.* **2017**, *12* (12), 1155−1160.
(54) Heckmann, J.; Scott, R.; Prudnikau, A. V.; Antanovich, A.; Owschimikow, N.; Artemyev, M.; Climente, J. I.; Woggon, U.; Grosse, N. B.; Achtstein, A. W. Directed Two-Photon Absorption in CdSe Nanoplatelets Revealed by k-Space Spectroscopy. *Nano Lett.* **2017**, *17* (10), 6321−6329.
(55) Planelles, J.; Achtstein, A. W.; Scott, R.; Owschimikow, N.; Woggon, U.; Climente, J. I. Tuning Intraband and Interband Transition Rates via Excitonic Correlation in Low-Dimensional Semiconductors. *ACS Photonics* **2018**, *5* (9), 3680−3688.
(56) Quick, M. T.; Owschimikow, N.; Khan, A. H.; Polovitsyn, A.; Moreels, I.; Woggon, U.; Achtstein, A. W. Two-photon based pulse autocorrelation with CdSe nanoplatelets. *Nanoscale* **2019**, *11* (37), 17293−17300.

https://dx.doi.org/10.1021/acsphotonics.0c00615
ACS Photonics 2020, 7, 2987−2994